AGU ADVANCING EARTH AND SPACE SCIENCES

JGR Solid Earth

RESEARCH ARTICLE
10.1029/2025JB033691

Enigmatic Harmonic Tremor in the Samail Ophiolite, Oman: Evidence for Subsurface Gas Flow

Tianze Liu[1], Chao Liang[2], John M. Aiken[3,4], Wenbo Wu[1,5], and Robert Sohn[1]

[1]Department of Geology and Geophysics, Woods Hole Oceanographic Institution, Woods Hole, MA, USA, [2]Institute for Disaster Management and Reconstruction, Sichuan University–The Hong Kong Polytechnic University, Chengdu, China, [3]Njord Centre, University of Oslo, Blindern, Norway, [4]Expert Analytics, Oslo, Norway, [5]Department of Earth and Planetary Science, University of California, Berkeley, CA, USA

Key Points:

- A harmonic tremor in the 25–191 Hz frequency band persisted for nine months at the Oman Drilling Project Multi-Borehole Observatory
- The tremor characteristics are inconsistent with known anthropogenic sources
- Gas migration in the subsurface fracture network is a plausible source mechanism, with important implications

Supporting Information:

Supporting Information may be found in the online version of this article.

Correspondence to:

T. Liu and C. Liang,
tianze.liu@whoi.edu;
chao.liang@scu.edu.cn

Citation:

Liu, T., Liang, C., Aiken, J. M., Wu, W., & Sohn, R. (2026). Enigmatic harmonic tremor in the Samail Ophiolite, Oman: Evidence for subsurface gas flow. *Journal of Geophysical Research: Solid Earth*, *131*, e2025JB033691. https://doi.org/10.1029/2025JB033691

Received 22 DEC 2025
Accepted 12 APR 2026

Author Contributions:

Conceptualization: Robert Sohn
Data curation: Tianze Liu, Robert Sohn
Formal analysis: Tianze Liu
Funding acquisition: Chao Liang, John M. Aiken, Robert Sohn
Investigation: Tianze Liu, Chao Liang, John M. Aiken, Wenbo Wu, Robert Sohn
Methodology: Tianze Liu, Chao Liang, Wenbo Wu
Project administration: Robert Sohn
Resources: Chao Liang, John M. Aiken, Robert Sohn
Software: Tianze Liu
Supervision: Robert Sohn
Visualization: Tianze Liu
Writing – original draft: Tianze Liu
Writing – review & editing: Tianze Liu, Chao Liang, John M. Aiken, Wenbo Wu, Robert Sohn

Abstract Harmonic tremors are a unique class of seismic signals often attributed to subsurface fluid flow, but can also be generated by anthropogenic processes. We present observations of a tremor with a harmonic interval of ∼12.75 Hz up to the 15th mode at ∼191 Hz during a seismic-borehole-acoustic experiment at the Oman Drilling Project Multi-Borehole Observatory, located on an ultramafic terrain of the Samail Ophiolite with minimal human activities. The tremor persisted for the entire 9-month observation interval, with mode frequencies varying by ∼0.1% diurnally and by ∼1% overall. We find that the tremor characteristics are inconsistent with signals from documented anthropogenic sources and that sustained gas flow through a fluid-filled, subsurface fracture is the most plausible source mechanism. Our results have potentially important implications for free gas processes during low-temperature serpentinization and motivate further research to investigate the seismic signals generated in these environments.

Plain Language Summary Harmonic tremors are a peculiar class of seismic signals consisting of narrow spectral peaks whose frequencies follow a harmonic relation, similar to the sounds of musical instruments and animal vocalization. The origins of harmonic signals are much debated, partly because they can be generated by both natural processes and human activities. Harmonic tremors are often observed in places where fluids move vigorously in the subsurface, such as active volcanoes. We observe a harmonic tremor that lasted 9 months in a formation comprised of rocks from Earth's upper mantle, where active fluid-rock reactions produce hydrogen and methane in the subsurface. We carefully examine the possible human activities that may cause the tremor and find that none can explain its properties. We conclude that the tremor is most likely generated by the sustained flow of free gas in the subsurface.

1. Introduction

Harmonic tremors are a class of seismic-acoustic signals with energy concentrated in narrow frequency bands that are integer multiples of a fundamental frequency ("harmonic modes"). In contrast to regular earthquakes, whose energy is concentrated in the time domain (short-lived) but distributed in the frequency domain (broadband), the energy of harmonic tremors is distributed in the time domain but concentrated in the frequency domain, making them difficult to analyze due to the lack of clear arrivals of seismic phases (i.e., P, S, and surface waves). The origin of harmonic tremors is elusive and sometimes controversial, as highlighted by a recent debate over the source of the tremors observed at a CO_2 injection site (Maher et al., 2024; Niyogi et al., 2023), because similar signals can result from both human activities and natural processes.

Harmonic tremors attributed to natural causes were first and still most commonly observed on active volcanoes (Benoit & McNutt, 1997; Hagerty et al., 2000; Hellweg, 2000; Hotovec et al., 2013; Ichihara et al., 2013; Maryanto et al., 2008; Schlindwein et al., 1995), where other types of tremors are also frequently detected (Konstantinou & Schlindwein, 2003). Other environments where harmonic tremors have been observed include glaciers (Röösli et al., 2014; Winberry et al., 2013), geysers (Nayak et al., 2020), and a hydrocarbon reservoir undergoing hydraulic fracturing (Tary et al., 2014). All these environments host active subsurface fluid flow. The proposed physical mechanisms for harmonic tremors of natural origins generally fall into three categories: (a) standing waves (resonances) in a fluid-filled cavity of finite dimensions (e.g., conduit or crack) (Chouet, 1988; Ferrazzini & Aki, 1987; Kumagai & Chouet, 2000), (b) traveling waves along fluid-filled cracks destabilized by rapid fluid flow (Balmforth et al., 2005; Dunham & Ogden, 2012; Julian, 1994), and (c) a series of transient

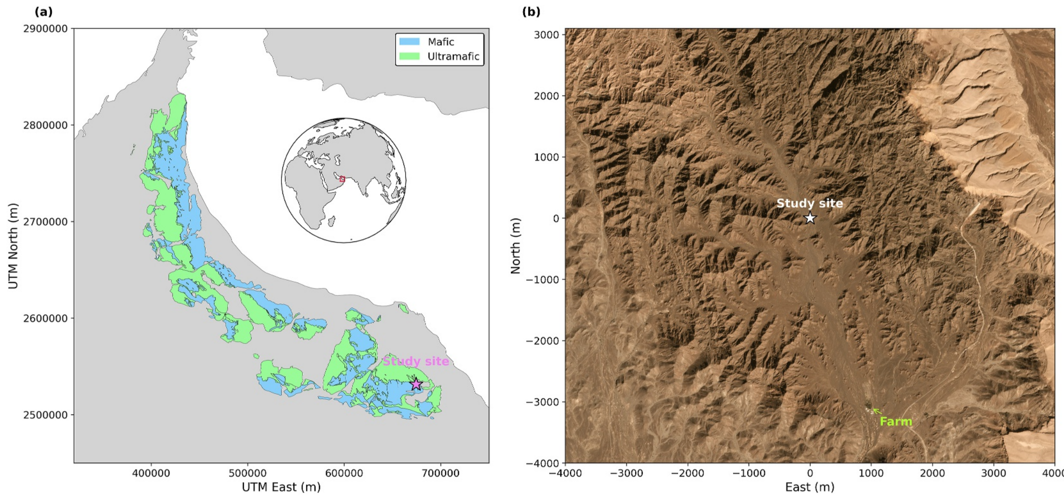

Figure 1. Study site location and surrounding environment. (a) Ultramafic and mafic units of the Samail Ophiolite (Nothaft, 2021) and the site location. (b) Satellite image of the area around the study site. The nearest human settlement, a farm ~3 km south of the site, is marked in green.

processes (e.g., frictional faulting events) with semi-regular reoccurrence intervals (Dmitrieva et al., 2013; Winberry et al., 2013).

Anthropogenic sources known to generate harmonic tremors include power generators and wind turbines, which generate harmonic signals with fundamental frequencies equal to the rotation rates of the rotors (Bilek et al., 2023; Marcillo & Carmichael, 2018), and transportation equipment, such as helicopters and freight trains, which generate harmonic signals with rapidly changing frequencies (i.e., "frequency gliding") (Li et al., 2018; Meng & Ben-Zion, 2018). In addition, data from seismic instruments deployed near high-voltage powerlines or powered by alternating current (AC) can contain "powerline noise," comprising a harmonic series with a fundamental frequency of 50 or 60 Hz, depending on the local AC frequency (Butler & Russell, 2003; Xia & Miller, 2000). These anthropogenic mechanisms can complicate the interpretation of harmonic signals in seismic records, especially if the records were obtained from sites near human activity.

Here, we present a harmonic tremor observed by a seismic and borehole-acoustic network deployed at the Oman Drilling Project (OmanDP) Multi-Borehole Observatory (MBO). The MBO was established to study processes associated with active serpentinization, an important and timely topic due to the capacity of ultramafic formations to absorb CO_2, produce hydrogen, and host chemosynthetic ecosystems (Kelemen & Matter, 2008; Osselin et al., 2022; Rempfert et al., 2017; Templeton & Caro, 2023; Zgonnik, 2020). We carefully examine the properties of the tremor and compare them with those expected for various anthropogenic and natural sources to assess the origin of the tremor.

2. Data and Methods

2.1. Study Site and Instrumentation

The OmanDP MBO is located on a peridotite terrain of the Samail Ophiolite in the Sultanate of Oman (Figure 1) and includes four ~400-m deep boreholes (BA1A–D), cased from the surface to ~20-m depth at the time of our experiment (Sohn & Matter, 2023), within a 200-by-200-m area in Wadi Laywani, a dry wash with an average water table depth of ~15 m (Figure 2) (Kelemen et al., 2021). The study site is located on the inactive NW-SE-striking Issmaiya Fault Zone (Callegari et al., 2022). In May 2019, two years after the holes were established and all downhole operations had concluded, we deployed two vertical hydrophone arrays with 70-m inter-element spacing, extending from 30 to 380 m depths in Boreholes BA1A and BA1B (Figure 2b), to monitor seismic activity for nine months until February 2020. The hydrophones were suspended in the borehole on a weighted cable and recorded borehole fluid pressure perturbations. For the final 21 days of the deployment, we augmented the hydrophone arrays with a dense network (~6 m minimum inter-element spacing) of oriented, three-component geophones that were organized in two subarrays, A and B, around BA1A and BA1B, respectively

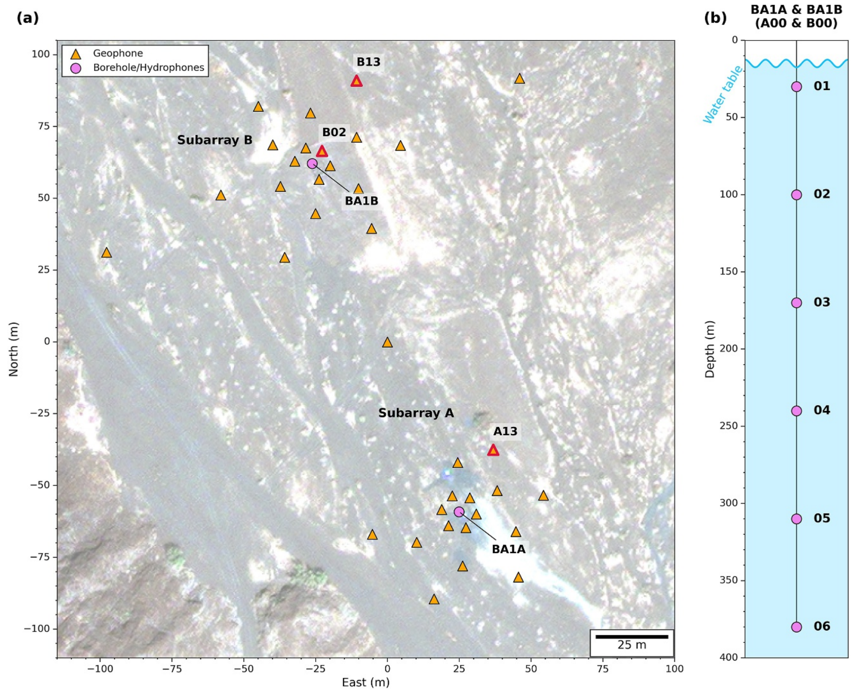

Figure 2. Site map (a) Boreholes and geophones plotted on a satellite image of the study site. Spectra of the highlighted geophones (red outlines) are shown in Figures 3 and 7, Figures S2 and S3 in Supporting Information S1. (b) Hydrophone depth profiles in the two boreholes.

(Figure 2a and Figure S1a in Supporting Information S1), with all hydrophones and geophones sampled at 1 kHz. The geophones were deployed on a low-seismic-velocity alluvium layer with a thickness varying from ∼20 m near BA1A to ∼0 m (basement outcropping) near BA1B (Kelemen et al., 2021). All geophones and the two hydrophone arrays operated independently and were powered by direct current (DC) supplied by solar panels (Figure S1 in Supporting Information S1).

The MBO site is located in a remote, mountainous region of the Omani desert accessible only by foot or off-road vehicles via several kilometers of dirt roads (Figure 1b and Figure S1a in Supporting Information S1). The nearest infrastructure is a road that crosses a ridge ∼2 km to the east and the nearest human settlement is a small farm ∼3 km to the south (Figure 1b). At the time of our experiment, there was no equipment of any kind on-site other than our instruments (Figure S1 in Supporting Information S1), but the site has subsequently been developed for carbon sequestration and presently hosts infrastructure to support this activity.

2.2. Data Analysis

2.2.1. Spectrogram Construction

We convert the raw hydrophone and geophone time series in digital counts to mPa and nm s^{-1}, respectively, using frequency-independent gains and divide the time series into non-overlapping 300-s (5 min) segments. We remove the linear trend from each segment, taper it using a Hanning window, and compute the power spectrum density using the Fast Fourier Transform, which yields a frequency sampling interval of 0.003 Hz. For the geophone data, we sum the spectra of the three components to produce a total power spectrum. We then construct the power spectrograms using all five-minute segments, which are used for visualization (Figure 3 and Figure S2 in Supporting Information S1), mode detection (Figures 4 and 5), and mode property extraction (Figure 6).

2.2.2. Mode Detection and Property Extraction

For the geophones, we detect a set of spectral peaks for each five-minute time window by finding the local maxima that satisfy two criteria: (a) a prominence, as defined in the SciPy function *scipy.find_peaks*, greater than 15 dB, and (b) a reverse-bandwidth, defined as the reciprocal of the peak width (less than 3 dB below the peak

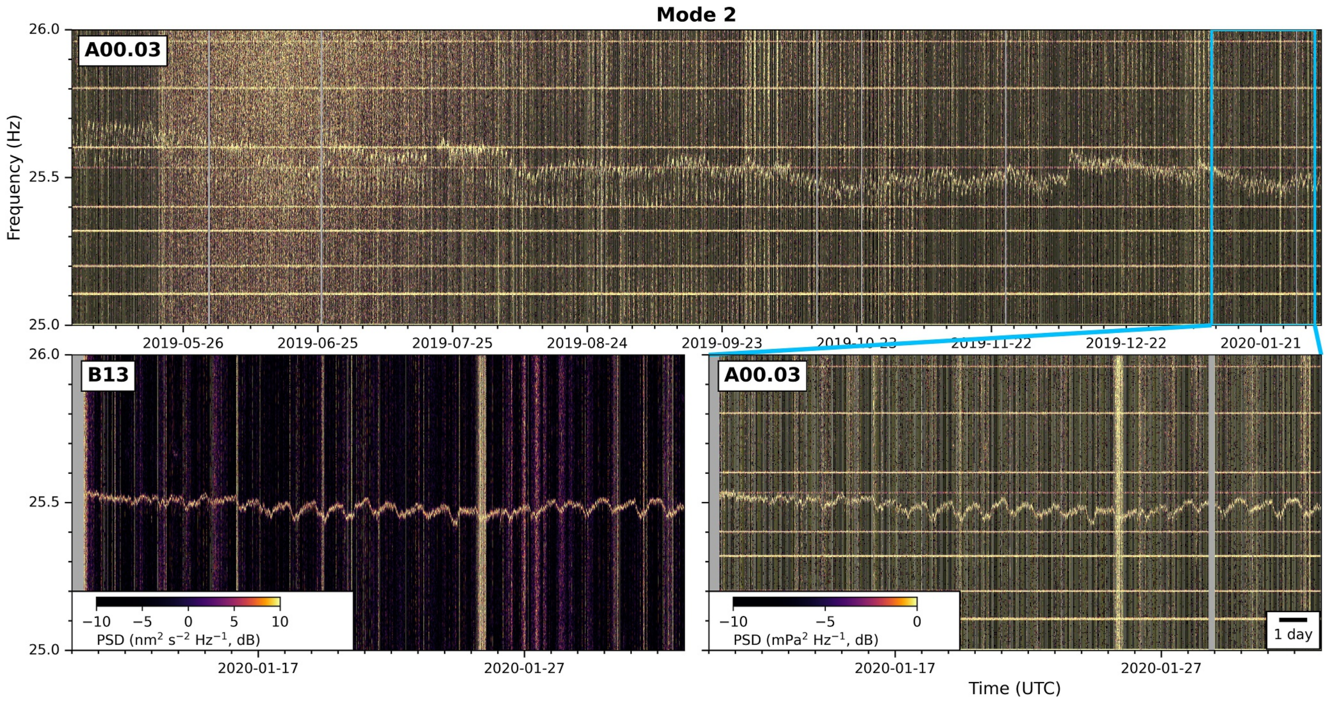

Figure 3. Power-density spectrograms of Mode 2. Top panel: Nine-month spectrogram of Mode 2 recorded on Hydrophone A00.03 (170 m depth in borehole; Figure 2). Bottom panels: 21-day spectrograms of Mode 2 recorded on Geophone B13 (left) and Hydrophone A00.03 (right). Horizontal lines in the hydrophone spectrograms are due to instrument noise. Data gaps are marked in gray.

power), greater than 15 Hz^{-1}, while excluding time windows with mean (frequency-averaged) spectral levels greater than 15 dB to prevent erroneous detections during intervals with strong background noise. We determine the frequency of each tremor mode in each time window by finding the frequency bin with the highest number of peak detections (i.e., detected by the most geophone stations) within an empirically determined range (Table S1 in Supporting Information S1) and note the mode power at these frequencies for each geophone (Figure 6). We compute the quality factor of a peak using:

$$Q_{\text{obs}} = \frac{f}{\Delta f} \tag{1}$$

where f and Δf are the peak frequency and bandwidth, defined as the frequency range where the power is above half (∼3 dB) of the peak power, respectively.

For the hydrophones, which have lower signal-to-noise ratios (SNRs), we use the data from the array in BA1A, which has better SNRs due to lower noise levels from borehole organpipe modes (Aiken et al., 2022), to extract the tremor modes. We detect spectral peaks using the same criteria as above except that (a) we use a −5 dB threshold to remove noisy time windows, (b) we remove spectral peaks with constant frequencies (horizontal lines in Figure 3 and Figure S2 in Supporting Information S1) that were caused by electrical noise, and (c) we only keep spectral peaks detected by at least three hydrophones. We start with the 21-day time window of the contemporaneous geophone data and identify the peaks at frequencies corresponding to the geophone mode frequencies. We then identify modal frequencies for each window prior to the geophone deployment by selecting the spectral peak closest to the mean modal frequency of the 10 nearest time windows, using a 0.075 Hz threshold to reject outliers. This method yields adequate mode detections from the hydrophone data despite the lower SNRs, revealing the modal frequency variations over the 9-month deployment.

2.2.3. Multi-Taper Autospectra of the Tremor Signal

The multi-taper method provides more robust (and computationally expensive) spectral estimates than the periodogram, and we use it for all subsequent spectral analyses, including the cross-spectral estimates described

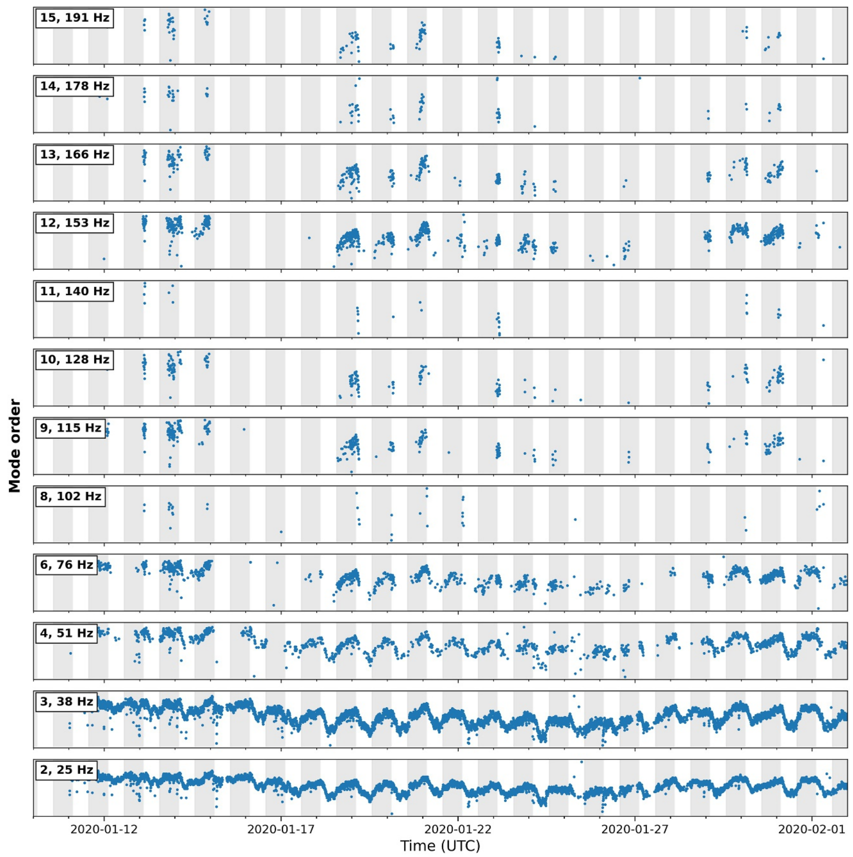

Figure 4. Temporal frequency variation for all modes detected from the spectrograms of all geophones. Text boxes contain the order and mean frequency of each mode. Each dot represents a detection of the mode. White and gray vertical stripes indicate daytime and nighttime intervals, respectively. See Section 2.2.2 for details of the mode-detection procedure.

in Section 2.2.4. We use the first five prolate spheroidal sequences with a time-half-bandwidth product (*NW*) of three as the tapers (Thomson, 1982). We use the multi-taper method to compute the total power spectral density (PSD) of the tremor signal recorded on Geophone A13 in the five minutes starting from 2020-01-13 19:50:00, UTC (Figure 7 and Figure S4 in Supporting Information S1). We use the same method to compute the PSDs of the signals recorded by Hydrophone B00.01 and Geophone B02 in the five minutes starting from 2020-01-20 08:00:00, UTC (Figure S3 in Supporting Information S1).

2.2.4. Multi-Taper Cross-Spectral Coherence and Phase Difference

We compute cross-spectral estimates of the squared coherence and phase difference of Mode 2, the lowest observed mode at ∼25 Hz, between adjacent geophone pairs in the network. We use 900-s (15-min) time windows for the cross-spectral analysis (three times the window length for computing the spectrograms) to increase the statistical quality of the estimates, and we only analyze the 15-min windows that include at least two 5-min windows with the mode detected on both stations. We estimate uncertainties of the cross-spectral parameters using jackknife resampling of values obtained for the five individual tapers. We select a 0.02-Hz wide frequency range centered around the average mode frequency for the 15-min window and extract the phase differences with coherences greater than 0.85 within this range. We compute the phase difference of the window by averaging the statistically independent phase differences (spaced $NW = 3$ frequency samples apart) weighted by the inverse of their uncertainties. Time windows with no qualifying phase differences are discarded. Because the tremor signals only exist in very narrow frequency bands, it is not possible to use the line-fitting method, which has been applied to broadband volcanic tremors (Barajas et al., 2024), to estimate the differential travel times between station pairs. Therefore, the estimated phase differences contain a cycle ambiguity, whose effects can be minimized by using only the phase differences of the signals of the lowest mode between closely spaced stations (Section 2.2.7).

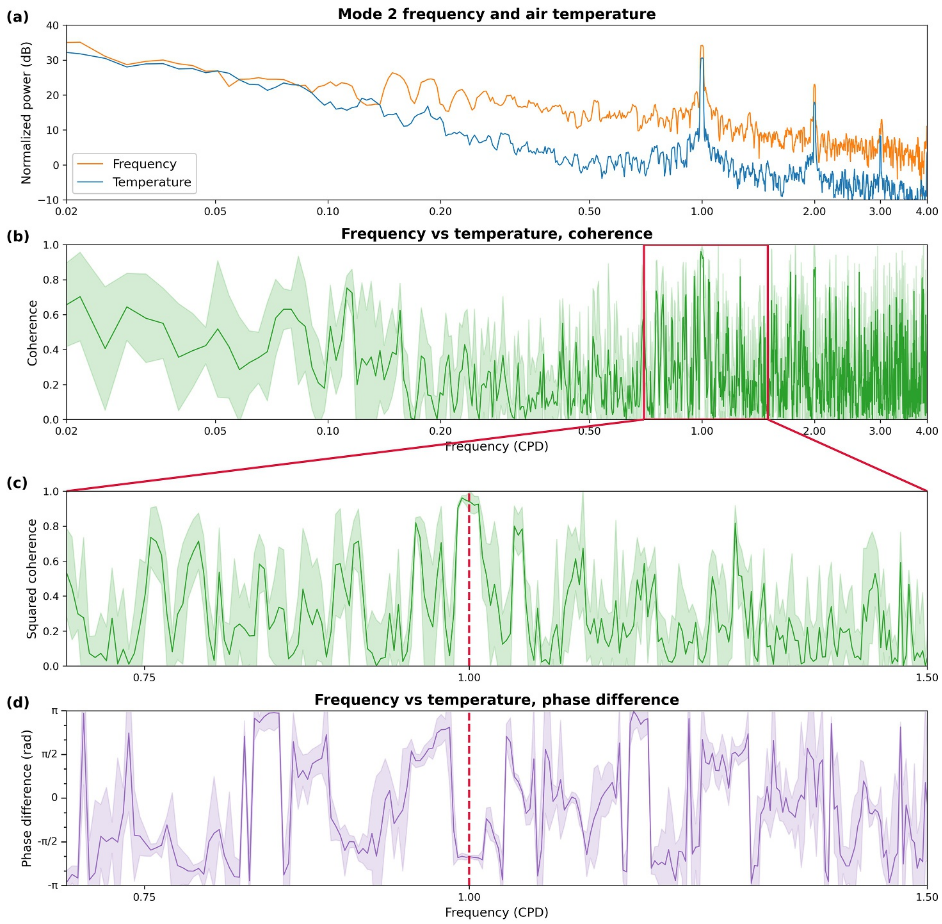

Figure 5. Cross-spectral analysis of Mode-2 frequency and air temperature. CPD: cycle-per-day. (a) Power spectral densities (Materials and Methods) of the frequency of Mode 2 (orange) and temperature (blue). (b) and (c) Squared cross-spectral coherence (green) between the frequency of Mode 2 and temperature in the ranges 0.02–4.00 CPD and 0.70–1.50 CPD, respectively. (d) Cross-spectral phase difference between the frequency of Mode 2 and temperature in the range 0.70–1.50 CPD. A positive phase difference indicates frequency leading temperature. Transparent colored areas indicate uncertainties.

2.2.5. Correlation Between Tremor Frequency and Air Temperature

The air temperature was contemporaneously measured in a recess on the hillside (just outside the boundary of Figure 2a) at 15-min intervals during our seismic experiment (Sohn & Matter, 2023). We use the multi-taper cross-spectral method described above to assess the correlation between the tremor frequency and air temperature for the 9-month interval of the hydrophone deployments. We use linear interpolation to up-sample the temperature to the 5-min sampling interval of the Mode 2 frequency estimates extracted from the hydrophone data and then compute the coherence and phase difference between the tremor frequency and the temperature using the multi-taper method (Figure 5).

2.2.6. Correlation Between the Powers of Different Modes

Among the 12 observed modes, Modes 2, 3, 4, 6, 9, 10, 12, and 13 are detected for enough time windows to enable meaningful power-correlation analyses. For each mode pair at each station, we select the time windows during which both modes are detected and compute the correlation between the dB values of the total powers of the two modes recorded within these time windows. The correlation values of all stations are then averaged to produce the averaged power-correlation values between each mode (Figure 6a).

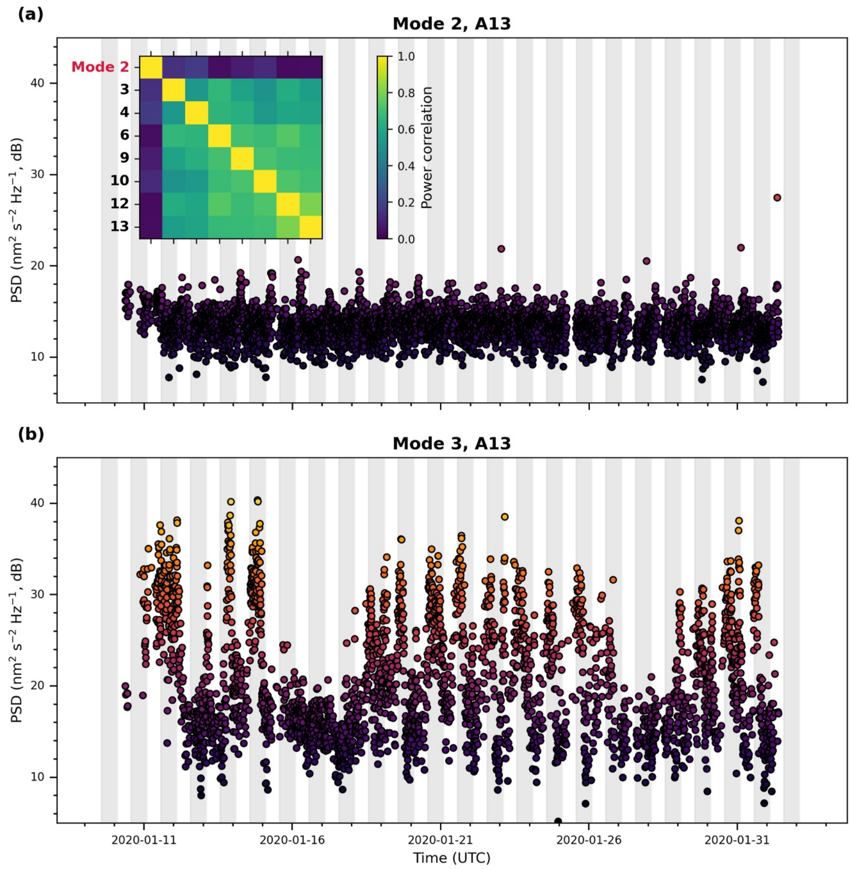

Figure 6. Mode power as a function of time at Geophone A13 for (a) Mode 2 and (b) Mode 3. Inset of (a) Correlation matrix of the power of a selected set of modes. White and gray vertical stripes indicate daytime and nighttime intervals, respectively.

2.2.7. Localizing the Tremor Source

Although the tremor signal lacks clear phase arrivals, we can use horizontal apparent velocity vectors estimated from phase differences between signals recorded on nearby stations to constrain the source location (Barajas et al., 2024; Nava et al., 2023), with the caveat that (a) the estimates are based on signals of likley multiple wave

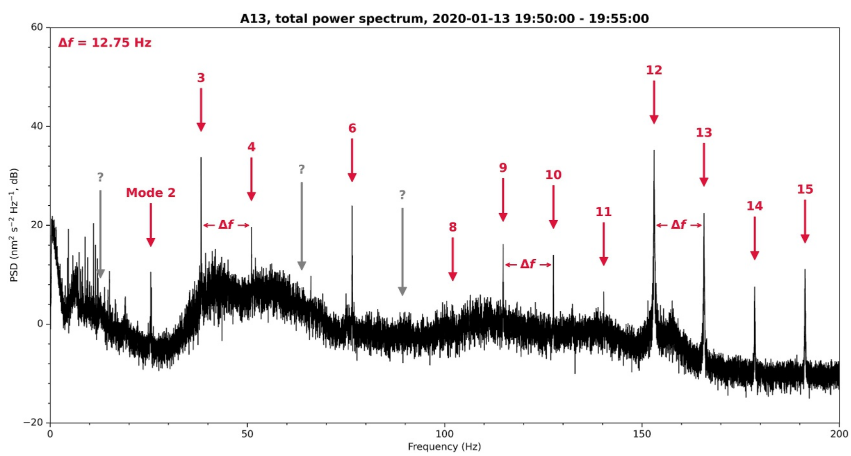

Figure 7. Total power spectral density (sum of the three components) of the signals recorded at Geophone A13 in a 5-min time window, with the observed and missing modes marked in red and gray, respectively. The regular frequency spacing of the modes, Δf, is shown for selected modes.

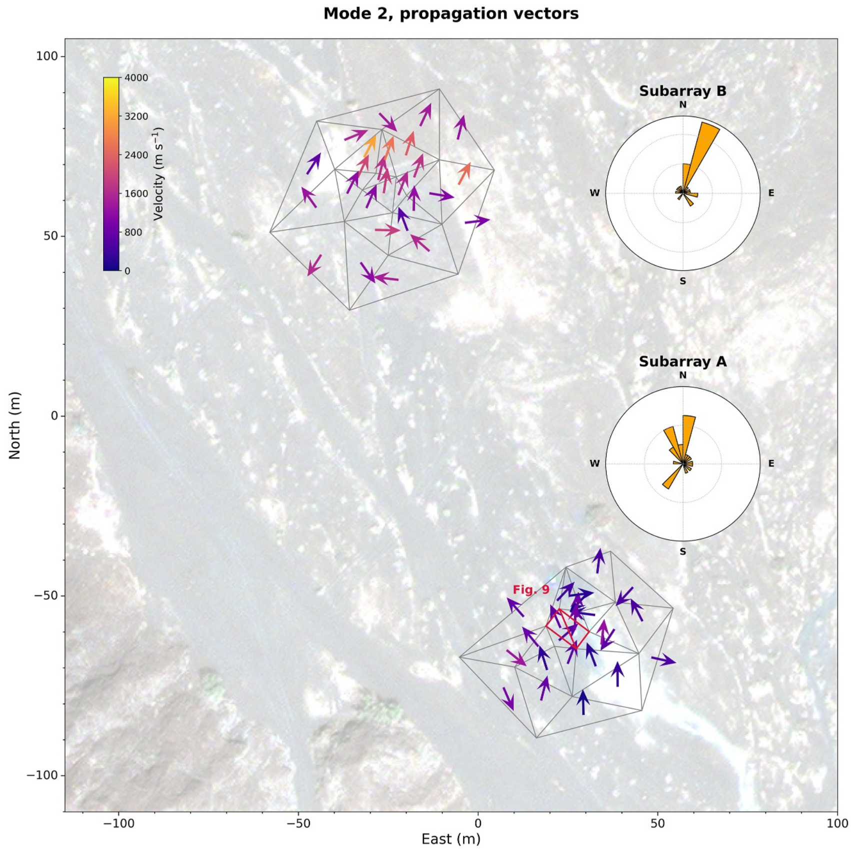

Figure 8. Horizontal apparent velocity vectors of Mode 2. The vectors are colored by absolute value and are plotted at the centers of the corresponding geophone triads. Rose diagrams: Distribution of the vector directions in the two subarrays. The temporal variations of the two triads highlighted in red are shown in Figure 9.

types (i.e., P, S, and surface waves), and (b) the phase-difference estimate, $\Delta\Phi$, contains a cycle ambiguity (e.g., the actual phase lag can be $\Delta\Phi \pm 2n\pi; n = 0, 1, 2\ldots$). To minimize the potential for cycle skipping, we use the lowest-frequency observed mode (Mode 2 at ~25 Hz) for the analysis and consider only closely spaced (<30 m) station pairs. This setting can avoid cycle skipping for waves with horizontal apparent velocities greater than ~750 m s^{-1}.

We organize the geophone network into Delauney triads (Figure 8) and convert the three-component phase-difference estimates described in Section 2.2.4 into travel-time differences for each geophone pair using:

$$\Delta t = \frac{\Delta\Phi}{2\pi f} \quad (2)$$

Assuming that the distance between the source and each triad is significantly greater than the triad dimension (<30 m), the wave field can be assumed to be locally planar, and the east and north components of the horizontal slowness vector of the triad (s_x and s_y) are related to the travel-time differences between the two station pairs forming the triad (Δt_{12} and Δt_{23}) by:

$$\begin{bmatrix} \Delta x_{12} & \Delta y_{12} \\ \Delta x_{23} & \Delta y_{23} \end{bmatrix} \begin{bmatrix} s_x \\ s_y \end{bmatrix} = \begin{bmatrix} \Delta t_{12} \\ \Delta t_{23} \end{bmatrix} \quad (3)$$

where Δx and Δy are the differences in the two geophones' east and north coordinates. We then solve the linear system to obtain the horizontal slowness vector for each data component of each geophone triad in each time window and convert it to a horizontal apparent-velocity vector (hereafter "propagation vector"), parametrized by

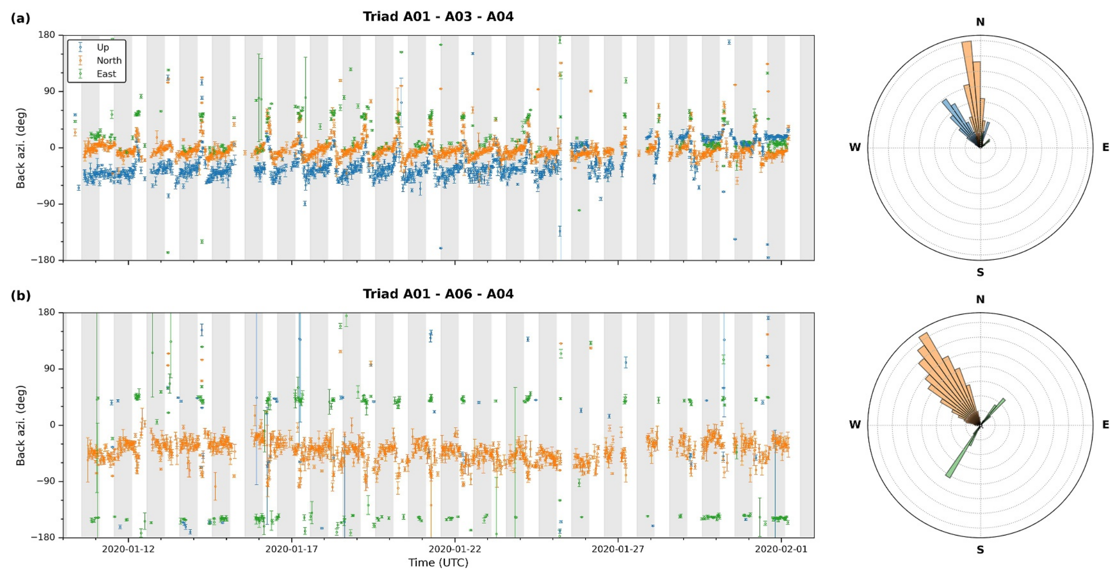

Figure 9. Temporal variation of propagation directions at two neighboring geophone triads (a) A01-A03-A04 and (b) A01-A06-A04 (Figure 8). Left: Propagation direction as a function of time and the associated uncertainties, estimated for the three components. Vertical stripes mark days and nights. Right: Rose diagram of the propagation directions in (a), colored accordingly.

an apparent velocity and a propagation direction (Figure 9). We calculate the uncertainties of the apparent velocities and propagation directions using the jackknife method. We finally obtain the time-averaged propagation vectors for each data component of each triad by taking the mean of the vectors of all time windows weighted by the reciprocals of the uncertainties. For each geophone triad, we show the time-averaged propagation vectors of the data component with the most qualifying time windows (Figures 8 and 9).

3. Results

3.1. Harmonic Modes and Frequency Variations

A careful inspection of the geophone and hydrophone spectrograms reveals the ubiquitous presence of signals with energy concentrated in narrow frequency bands. Many of these signals are transient, but here we focus on a harmonic sequence (hereafter "harmonic tremor") with a frequency spacing of ~12.75 Hz that persisted for the entire 9-month hydrophone deployment (Figure 3 and Figure S2 in Supporting Information S1). The harmonic signal is strongest in the geophone data, where it can be intermittently detected up to the 15th mode at ~191.3 Hz (Figure 4), and the lowest two observed modes, Modes 2 and 3 at ~25.5 and ~38.3 Hz, respectively, are continuously detected in both the 21-day geophone records and the 9-month hydrophone records (Figures 3 and 4, and Figure S2 in Supporting Information S1). All modes are detected at the same frequencies by all instruments (geophones and hydrophones) (Figure 3 and Figure S2 in Supporting Information S1), indicating that they are not caused by wave-propagation effects, such as resonances in a near-surface low-velocity layer. We are unable to detect the putative first (fundamental), fifth, and seventh modes in any of the records (Figure 7), similar to the mode structure reported for harmonic tremors observed on the Mt Semeru Volcano in Indonesia (Schlindwein et al., 1995).

The mode frequencies exhibit a subtle yet robust temporal variation that is synchronized across modes and independently operating instruments (Figures 3 and 4, and Figure S2 in Supporting Information S1). The frequency variation includes a regular diurnal oscillation of ~0.1% that is highly correlated with air temperature (Figure 5) and a larger, more gradual variation of ~1% over the 9-month hydrophone deployment (Figure 3 and Figure S2 in Supporting Information S1) that is not correlated with air temperature or other known environmental parameters. The mode frequencies are distinct from those generated by standing waves in the borehole water column (e.g., St-Onge & Eaton, 2011), which have a fundamental mode at ~1 Hz and are clearly observed in the hydrophone data but not in the geophone data (Figure S3 in Supporting Information S1; Text in Supporting

Information S1), indicating that the borehole resonances do not radiate significant energy into the surrounding formation.

3.2. Mode Power and Quality Factors

Our analysis of the 21-day geophone data reveals that the signal power of Modes 3 and above is correlated, but the power of Mode 2, the lowest mode observed, is decorrelated with all other modes (Figure 6a). This decorrelation between mode power has also been reported for the harmonic tremors observed on the Mt Semeru Volcano (Schlindwein et al., 1995). The power of Mode 2 is relatively constant (±5 dB) and typically peaks during daytime (Figure 6a), whereas the power of Mode 3 is more variable (±15 dB) and typically peaks during nighttime (Figure 6b). In addition, the power of Modes 3 and above is elevated during the multi-day intervals of January 10–15, January 18–26, and January 29–February 1 (Figure 6b). No apparent correlation between the mode power and environmental factors is observed. The quality factors measured for the Mode 2 signal from spectral peak widths are unusually high, ranging between 1,000 and 4,000. Unlike the power of Mode 3 and above, the quality factor of Mode 2 exhibits no systematic temporal variation.

3.3. Tremor Propagation Vectors and Source Location

The time-averaged propagation vectors exhibit spatial variablility, but overall, the propagation vectors for Subarray B point north-northeast, whereas those for Subarray A point north (Figure 8). The apparent velocities for Subarray A (<1,000 m s^{-1}) are lower than those for Subarray B (up to 3,500 m s^{-1}; Figure 8), consistent with the local near-surface structure (~20 m thick low-velocity alluvium layer surrounding Hole BA1A vs. basement outcropping at Hole BA1B), indicating that the tremor signal consists of both fast body waves traveling in the basement and slow surface waves traveling in the alluvium layer.

The spatial variability of the time-averaged propagation directions is unlikely to result from statistical errors but rather reflects complexities in source radiation and wave propagation since the statistical uncertainties of individual time windows (typically <10°) are much smaller than the differences between the time-averaged results for different triads (Figures 8 and 9). Propagation directions estimated from different data components in a single triad can vary (Figure 9), likely because the signal contains a mixture of different wave types (P, S, and surface waves), which have different particle motions and can propagate in different directions due to source and path effects. Intriguingly, the estimated propagation directions for some geophone triads show systematic diurnal variations that are greater than the statistical uncertainties (Figure 9). This diurnal variation is more pronounced in Subarray A than in Subarray B, consistent with a source located closer to Subarray A. This feature is similar to the temporal variation of particle motions of the harmonic tremors observed on the Arenal Volcano in Costa Rica, which was interpreted as resulting from a change in source depth (Benoit & McNutt, 1997; Hagerty et al., 2000).

Overall, our propagation vectors indicate that the tremor source is to the south, or within the southern edge, of the seismic network. The observation of strong high-frequency modes (>150 Hz; Figure 7), whose power attenuates quickly during propagation, suggests a local source. Near-field effects could also contribute to the spatial variability of the propagation vectors (e.g., non-planar wavefronts), particularly for Subarray A.

4. Discussion

The seismic and borehole-acoustic data from the MBO site contain a harmonic sequence of resonances that persisted for the entire 9-month observation interval. The harmonic series has a frequency spacing of ∼12.75 Hz and continues up to the 15th mode at ∼191.3 Hz, but lacks the first, fifth, and seventh modes. The resonance peaks have unusually high quality factors (>1,000) and exhibit subtle yet robust frequency variation with time, including a consistent diurnal variation of ∼0.1%. This unique set of characteristics raises questions regarding the source mechanism and whether it was generated by anthropogenic or natural sources.

4.1. Potential Anthropogenic Sources

The high quality factors of the resonant modes and the observation that the frequency spacing (12.75 Hz) is nearly an integer fraction (1/4) of the AC frequency in Oman (50 Hz) are suggestive of an anthropogenic source. We can rule out powerline noise (e.g., Xia & Miller, 2000) because all instruments were powered by DC, the nearest powerline at the time of the observations was more than 3 km away, and the tremor signal propagates across the array at elastic wave speeds (Figure 8), indicating they are not generated by electromagnetic perturbations. We can also rule out transportation equipment because it generates transient signals (typically seconds to minutes) with rapidly changing frequencies (Li et al., 2018; Meng & Ben-Zion, 2018), inconsistent with the characteristics of the MBO tremor.

The most probable anthropogenic source mechanism for the MBO tremor is a machine with components that rotate at a near-constant rate. Large-scale power-generating facilities, such as wind turbines and hydroelectric plants, can generate narrow-band seismic signals that can be detected by seismometers tens to hundreds of kilometers away (Bokelmann & Baisch, 1999; Hjortenberg & Risbo, 1975; Marcillo & Carmichael, 2018; Marcillo & MacCarthy, 2020), and the frequency of the signals can vary slightly over time due to fluctuations in the power grid's load, which affects the rotation rates (Hjortenberg & Risbo, 1975). At a smaller scale, diesel-powered generators and water pumps can generate harmonic signals detectable at shorter distances (e.g., ∼100 m) (Bilek et al., 2023).

The closest large-scale power-generating facility is the Al Kamil natural-gas power plant (285 MW), which is ∼66 km southeast of the MBO site (https://aenert.com/countries/asia/energy-industry-in-oman/), and the nearest possible location for a machine of any kind is a small (∼500-by-200 m) farm ∼3 km to the south (Figure 1). Machines at both sites could in principle generate detectable ground motions at the MBO site, but the mode structure is difficult to reconcile with the MBO observations. Power spectra from machines typically contain a high-power peak at the fundamental frequency, followed by a harmonic sequence, whose powers decrease near-monotonically with frequency (Figure S4 in Supporting Information S1). The overtones also experience higher attenuation during propagation with increasing frequency, which, combined with their lower power, often makes them difficult to identify at a distance. Studies of seismic signals from large-scale power-generating facilities usually detected only the fundamental modes at <10 Hz (Bokelmann & Baisch, 1999; Hjortenberg & Risbo, 1975), and in the case of the small generator-pump system described in Bilek et al. (2023), the power of the overtone at ∼185 Hz drops close to the noise floor at a distance of only ∼100 m from the source (Figure S4 in Supporting Information S1). In contrast, the MBO tremor contains strong overtones at frequencies >150 Hz, which can be stronger than Mode 2 (Figure 7 and Figure S4 in Supporting Information S1). If we assume that the tremor source is a machine located at the farm 3 km away and use a quality factor of 30, which was estimated for fractured granite in the top 3-km depth (Abercrombie, 1997), to extrapolate the power of each mode to the source location, Mode 12 will be ∼80 dB stronger than Mode 2 (Figure S4 in Supporting Information S1). This mode structure is inconsistent with that of documented signals generated by machines with rotating components.

Moreover, since the rotating components in machines generate harmonic seismic signals through repeating processes, the powers of different modes are expected to vary coherently, which is inconsistent with the decorrelation between the power of Mode 2 and other modes of the MBO tremor (Figure 6a). The observation that the power of the modes higher than two is higher during nighttime than daytime (Figure 6) is also inconsistent with power grid's load variation. Finally, a distant machine cannot generate signals with time-varying propagation directions (Figure 9). Although we cannot rule out an anthropogenic source that produces a previously undocumented type of seismic signal, the characteristics of the MBO tremor are inconsistent with signals from known human activities.

4.2. Potential Natural Sources

The MBO tremor shares several key features (complex mode structure, decorrelated mode-power variations, and apparent source movement) with volcanic harmonic tremors (Benoit & McNutt, 1997; Schlindwein et al., 1995), suggesting that it may be generated by subsurface fluid flow. The flow-instability model is unlikely due to the high flow speed required (on the order of 10–100 m s^{-1}) (Balmforth et al., 2005; Julian, 1994). The repeating-event model is implausible because the repeating events would have to occur at a high rate of ∼12 per second and persist for nine months and is inconsistent with the observed decorrelation of Mode 2 power with the other modes (Figure 6a). Ongoing serpentinization at the MBO site produces hydrogen- and methane-rich alkaline fluids (Kelemen et al., 2021; Nothaft et al., 2021), with some of the hydrogen and methane migrating as free gas through the pervasive fracture network in the formation, as evidenced by episodic gas bubble releases into Borehole BA1B during the hydrophone deployment (Aiken et al., 2022). Continuous discharge of gas bubbles is also observed in hyperalkaline springs in the Samail Ophiolite (Leong et al., 2023), which are likely supplied by

10.1029/2025JB033691

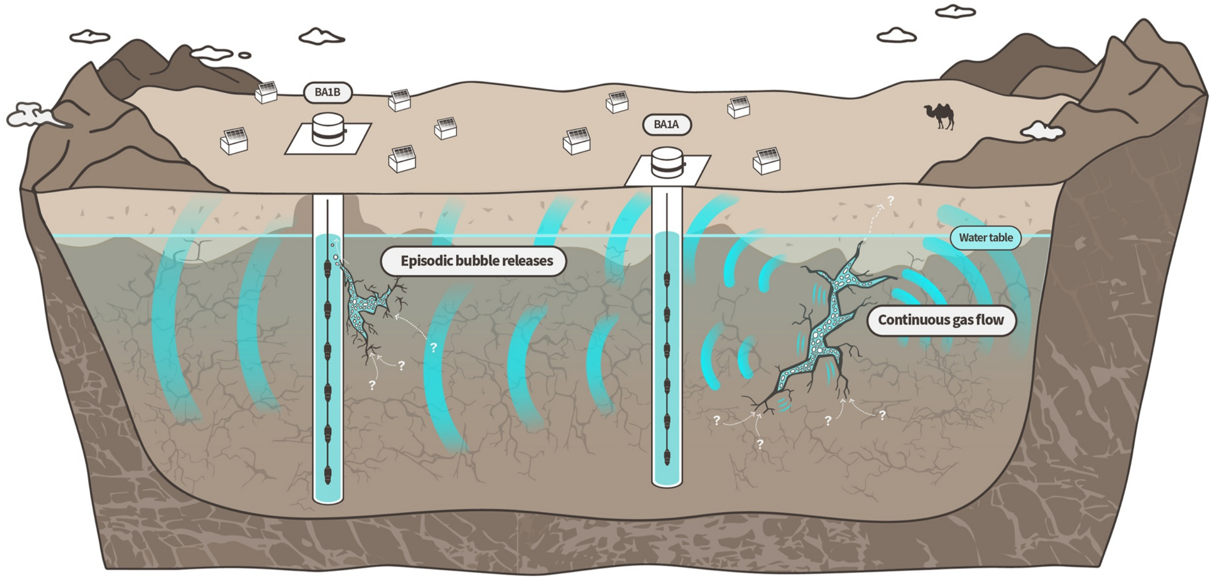

Figure 10. Conceptual illustration of subsurface gas flow at the MBO site inferred from seismic and borehole-acoustic observations. Free gas migration, both episodically and continuously, generates seismic and acoustic signals detected by borehole hydrophones and surface geophones. Objects are not to scale.

similarly continuous gas flow in the subsurface. The continuous flow of free gas bubbles through a water-filled fracture near the MBO site is thus a plausible mechanism for the tremor (Figure 10).

The evenly spaced harmonic modes of the MBO tremor indicate that the waves forming the resonances are non-dispersive acoustic waves. This observation is consistent with theoretical predictions that the high compressibility of the gas-water mixture in the fracture will cause waves propagating along the fracture to approach the sound-wave limit, where the propagation velocity equals the sound speed of the fluid mixture and is frequency-independent (Lipovsky & Dunham, 2015). Although the precise shape of the fracture cannot be constrained with our observations, the evenly spaced modes suggest that they are caused by resonances along a certain dimension of the fracture, whose length scale can be estimated using the simple acoustic-resonance model described below.

Considering the acoustic resonance of a fracture filled with a water-gas mixture, its fundamental frequency f_0 is determined by the fracture dimension, L, and the effective sound speed of the mixture, c_{eff}:

$$f_0 = c_{\mathrm{eff}}/2L. \tag{4}$$

The effective sound speed of the two-phase fluid in the fracture and the quality factor of its resonance are both controlled by the volume fractions of the phases and the fluid pressure, which is closely related to source depth (Figure 11; Text in Supporting Information S1). The plausible depth range for a fluid-filled fracture at the MBO site extends approximately from the water table at ∼15 m depth (Kelemen et al., 2021) to a depth of ∼150 m, where a steep reduction in formation permeability is observed (Katayama et al., 2020; Lods et al., 2020). For source depths of 15 and 150 m, the observed quality factors and resonant frequencies yield gas volume fractions of 0.76–0.95 and 0.95–0.99 and fracture dimensions of 2–4 m and 9–23 m, respectively (Figure 11; Text in Supporting Information S1). Fractures of such dimensions are likely present in the subsurface near the study site due to its location in the Issmaiya Fault Zone (Callegari et al., 2022) and the likely role of fault zones in facilitating the migration of hydrogen in the Samail Ophiolite (Pasquet et al., 2024). The resonance of the fracture is forced by the acoustic signals generated by the continuous flow of the two-phase fluid through the fracture, whose spectrum determines the observed mode structure (lack of a fundamental, large high-frequency amplitudes; Figure 7). Temporal variations in the forcing spectrum could also explain the observed decorrelation between the power of Mode 2 and other modes. Given the strong high-frequency signals of the tremor, the fracture is probably located very close to the study site.

The correlation between the tremor frequency and air temperature (Figure 5) suggests that thermal effects modulate the tremor frequency. Diurnal surface temperature perturbations at the study site do not penetrate to

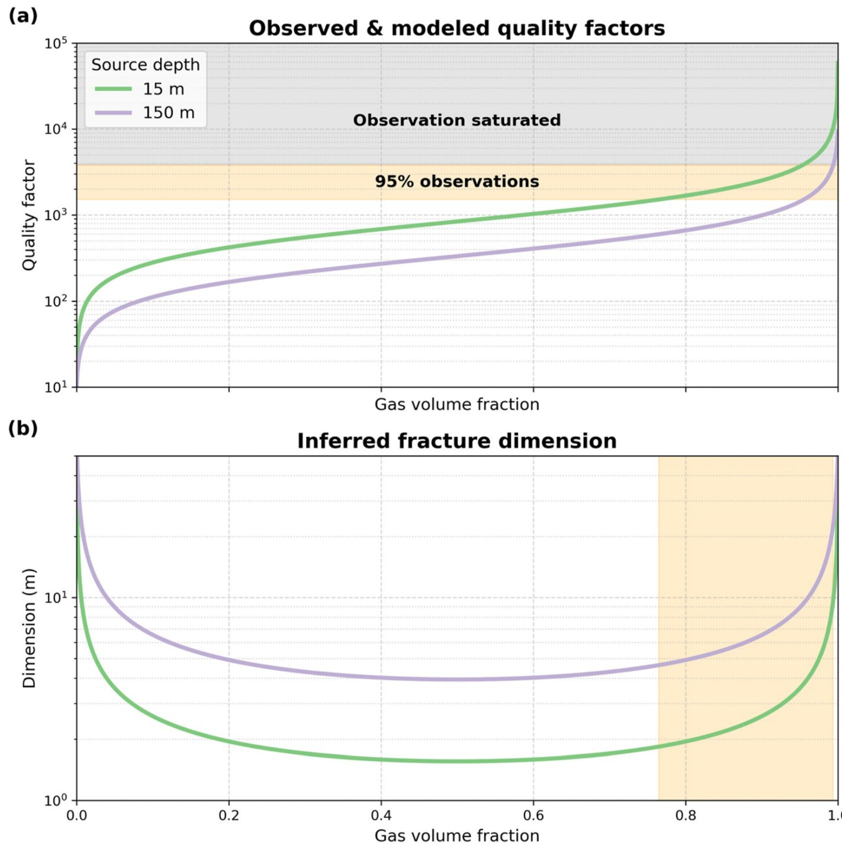

Figure 11. Inferring the source properties from the observed tremor frequencies and quality factors (a) Observed and modeled quality factors of the tremor source as a function of hydrogen volume fraction and source depth. Orange and gray shaded areas: quality-factor ranges containing 95% of the observations for Mode 2 and those beyond the resolution limit, respectively. (b) Inferred fracture dimensions as a function of hydrogen volume fraction and source depth. A fundamental frequency of 12 Hz is assumed. Orange shaded area: gas-volume-fraction range inferred from the quality factor range in (a).

depths greater than ~1 m, but the thermoelastic strain caused by uneven surface heating can extend much deeper (Berger, 1975). We find that the thermolelastic strain caused by a diurnal surface temperature variation of 10 K with horizontal wavelengths of 10^2–10^4 m produces fractional pressure changes of 10^{-3} to 10^{-2} within the 15–150 m depth range (Figure S5 in Supporting Information S1; Text in Supporting Information S1). These pressure perturbations are sufficient to generate the observed ~0.1% fractional variations in tremor frequency by altering the effective sound speed of the fluid mixture within the fracture and/or by modifying the fracture dimensions.

4.3. Implications of the Source Mechanism

The resonating-fracture mechanism requires a sustained flow of free gas through a well-established path, which has important implications for the hydrogen resource potential of ultramafic formations (Templeton et al., 2024) and for the biological processes they host (Ellison et al., 2021; Rempfert et al., 2017). Dissolved gas concentrations measured in the fluids of Hole BA1A were below saturation levels at all depth intervals (Nothaft et al., 2021), suggesting that free gas is not widespread in the formation. However, episodic bubble discharge into Hole BA1B was observed during our experiment (Aiken et al., 2022), and continuous bubble streams are found in hyperalkaline springs in the area (Leong et al., 2023), providing clear evidence that free gas exists and migrates in the subsurface. These observations can be reconciled if the free gas migrating through the fracture network is out of equilibrium with the liquid phase, perhaps due to kinetic inhibition (Figure 10). Intriguingly, a diurnal variation in surface hydrogen flux has been reported on a “fairy circle” in Brazil (Moretti et al., 2021), similar to the diurnal power variation of the MBO tremor (Figure 6), which could also be caused by a diurnal variation in gas flux through the fracture.

4.4. Summary and Outlook

We observe a harmonic tremor at the Muti-Borehole Observatory of the Oman Drilling Project, which persisted for the entire 9-month observation interval. We find the most plausible source mechanism to be sustained subsurface gas migration through the fracture network near the site. Our results, combined with those from previous studies, suggest that the migration of free gas produced by serpentinization in ultramafic formations may be vigorous enough to generate detectable seismic and acoustic signals, motivating further seismic and borehole-acoustic studies to investigate these processes.

Conflict of Interest

The authors declare no conflicts of interest relevant to this study.

Availability Statement

The seismic and borehole-acoustic data are publicly available through the Seismological Facility for the Advancement of Geoscience (SAGE) under the network code 7F (Sohn, 2022). The software used to analyze the data and generate the plots in the paper is publicly available on GitHub (Liu & Mellon, 2026). The geological map of the Samail Ophiolite is from the University of Colorado Boulder (Nothaft, 2021).

Acknowledgments
Drilling in the Oman Drilling Project was supported by the Alfred P. Sloan Foundation (in association with the Deep Carbon Observatory, DCO), the International Continental Scientific Drilling Program (ICDP), US National Science Foundation (NSF) Grant EAR-1516300, the Japanese Marine Science and Technology Center (JAMSTEC), and the Japan Society for the Promotion of Science Grant 16H06347, and contributions from the Sultanate of Oman Ministry of Regional Municipalities and Water Resources, the Oman Public Authority for Mining, and Sultan Qaboos University. The analyses presented in this paper were funded by the NSF Grant EAR-2147529, the National Natural Science Foundation of China Grant 42574118, and the Norwegian Research Council Grant 334395 (SerpRateAI). We thank Planet Labs for providing satellite images for free. We gratefully acknowledge Paul Fucile for instrumentation and fieldwork, Jüerg Matter for logistics and fieldwork, Benoit Cordonnier for fieldwork, and the Earthquake Monitoring Center of Sultan Qaboos University (Issa El-Hussain, Director) for technical support. The manuscript has benefited from insightful discussions with François Renard, Peter Kelemen, Nicholas Harmon, Catherine Rychert, and Matěj Peč.

References

Abercrombie, R. E. (1997). Near-surface attenuation and site effects from comparison of surface and deep borehole recordings. *Bulletin of the Seismological Society of America*, *87*(3), 731–744. https://doi.org/10.1785/BSSA0870030731

Aiken, J. M., Sohn, R. A., Renard, F., Matter, J., Kelemen, P., & Jamtveit, B. (2022). Gas migration episodes observed during peridotite alteration in the Samail ophiolite, Oman. *Geophysical Research Letters*, *49*(21), e2022GL100395. https://doi.org/10.1029/2022GL100395

Balmforth, N. J., Craster, R. V., & Rust, A. C. (2005). Instability in flow through elastic conduits and volcanic tremor. *Journal of Fluid Mechanics*, *527*, 353–377. https://doi.org/10.1017/S0022112004002800

Barajas, A., Shapiro, N. M., & Prieto, G. (2024). Differential phase analysis for volcanic tremor detection and source location. *Journal of Geophysical Research: Solid Earth*, *129*(10), e2024JB029010. https://doi.org/10.1029/2024JB029010

Benoit, J. P., & McNutt, S. R. (1997). New constraints on source processes of volcanic tremor at arenal volcano, Costa Rica, using broadband seismic data. *Geophysical Research Letters*, *24*(4), 449–452. https://doi.org/10.1029/97GL00179

Berger, J. (1975). A note on thermoelastic strains and tilts. *Journal of Geophysical Research*, *80*(2), 274–277. https://doi.org/10.1029/JB080i002p00274

Bilek, S. L., Luhmann, A. J., Grapenthin, R., Woo, H. B., & Gochenour, J. A. (2023). Capturing seismic signals from karst aquifer injection experiments and a natural recharge event. *Journal of Geophysical Research: Solid Earth*, *128*(4), e2022JB025635. https://doi.org/10.1029/2022JB025635

Bokelmann, G. H. R., & Baisch, S. (1999). Nature of narrow-band signals at 2.083 Hz. *Bulletin of the Seismological Society of America*, *89*(1), 156–164. https://doi.org/10.1785/BSSA0890010156

Butler, K. E., & Russell, R. D. (2003). Cancellation of multiple harmonic noise series in geophysical records. *Geophysics*, *68*(3), 1083–1090. https://doi.org/10.1190/1.1581080

Callegari, I., Scharf, A., Mattern, F., & Scharf, K. (2022). Tectonic transition from thrusting to polyphase non-confining deformation within the semail ophiolite along the sinistral, transtensional issmaiya fault zone (sultanate of Oman). *Journal of Asian Earth Sciences*, *224*, 105007. https://doi.org/10.1016/j.jseaes.2021.105007

Chouet, B. (1988). Resonance of a fluid-driven crack: Radiation properties and implications for the source of long-period events and harmonic tremor. *Journal of Geophysical Research*, *93*(B5), 4375–4400. https://doi.org/10.1029/JB093iB05p04375

Dmitrieva, K., Hotovec-Ellis, A. J., Prejean, S., & Dunham, E. M. (2013). Frictional-faulting model for harmonic tremor before redoubt volcano eruptions. *Nature Geoscience*, *6*(8), 652–656. https://doi.org/10.1038/ngeo1879

Dunham, E. M., & Ogden, D. E. (2012). Guided waves along fluid-filled cracks in elastic solids and instability at high flow rates. *Journal of Applied Mechanics*, *79*(3), 031020. https://doi.org/10.1115/1.4005961

Ellison, E. T., Templeton, A. S., Zeigler, S. D., Mayhew, L. E., Kelemen, P. B., & Matter, J. M., & The Oman Drilling Project Science Party. (2021). Low-temperature hydrogen formation during aqueous alteration of serpentinized peridotite in the samail ophiolite. *Journal of Geophysical Research: Solid Earth*, *126*(6), e2021JB021981. https://doi.org/10.1029/2021JB021981

Ferrazzini, V., & Aki, K. (1987). Slow waves trapped in a fluid-filled infinite crack: Implication for volcanic tremor. *Journal of Geophysical Research*, *92*(B9), 9215–9223. https://doi.org/10.1029/JB092iB09p09215

Hagerty, M. T., Schwartz, S. Y., Garcés, M. A., & Protti, M. (2000). Analysis of seismic and acoustic observations at arenal volcano, Costa Rica, 1995–1997. *Journal of Volcanology and Geothermal Research*, *101*(1–2), 27–65. https://doi.org/10.1016/S0377-0273(00)00162-1

Hellweg, M. (2000). Physical models for the source of Lascar's harmonic tremor. *Journal of Volcanology and Geothermal Research*, *101*(1–2), 183–198. https://doi.org/10.1016/S0377-0273(00)00163-3

Hjortenberg, E., & Risbo, T. (1975). Monochromatic components of the seismic noise in the NORSAR area. *Geophysical Journal of the Royal Astronomical Society*, *42*(2), 547–554. https://doi.org/10.1111/j.1365-246X.1975.tb05877.x

Hotovec, A. J., Prejean, S. G., Vidale, J. E., & Gomberg, J. (2013). Strongly gliding harmonic tremor during the 2009 eruption of redoubt volcano. *Journal of Volcanology and Geothermal Research*, *259*, 89–99. https://doi.org/10.1016/j.jvolgeores.2012.01.001

Ichihara, M., Lyons, J. J., & Yokoo, A. (2013). Switching from seismic to seismo-acoustic harmonic tremor at a transition of eruptive activity during the Shinmoe-dake 2011 eruption. *Earth Planets and Space*, *65*(6), 633–643. https://doi.org/10.5047/eps.2013.05.003

Julian, B. R. (1994). Volcanic tremor: Nonlinear excitation by fluid flow. *Journal of Geophysical Research*, *99*(B6), 11859–11877. https://doi.org/10.1029/93JB03129

Katayama, I., Abe, N., Hatakeyama, K., Akamatsu, Y., Okazaki, K., Ulven, O. I., et al. (2020). Permeability profiles across the crust-mantle sections in the Oman drilling project inferred from dry and wet resistivity data. *Journal of Geophysical Research: Solid Earth*, *125*(8), e2019JB018698. https://doi.org/10.1029/2019JB018698

Kelemen, P. B., Leong, J. A., Carlos De Obeso, J., Matter, J. M., Ellison, E. T., Templeton, A., et al. (2021). Initial results from the Oman drilling project multi-borehole observatory: Petrogenesis and ongoing alteration of mantle peridotite in the weathering horizon. *Journal of Geophysical Research: Solid Earth*, *126*(12), e2021JB022729. https://doi.org/10.1029/2021JB022729

Kelemen, P. B., & Matter, J. (2008). In situ carbonation of peridotite for CO_2 storage. *Proceedings of the National Academy of Sciences*, *105*(45), 17295–17300. https://doi.org/10.1073/pnas.0805794105

Konstantinou, K. I., & Schlindwein, V. (2003). Nature, wavefield properties and source mechanism of volcanic tremor: A review. *Journal of Volcanology and Geothermal Research*, *119*(1–4), 161–187. https://doi.org/10.1016/S0377-0273(02)00311-6

Kumagai, H., & Chouet, B. A. (2000). Acoustic properties of a crack containing magmatic or hydrothermal fluids. *Journal of Geophysical Research*, *105*(B11), 25493–25512. https://doi.org/10.1029/2000JB900273

Leong, J. A., Nielsen, M., McQueen, N., Karolytė, R., Hillegonds, D. J., Ballentine, C., et al. (2023). H2 and CH4 outgassing rates in the samail ophiolite, Oman: Implications for low-temperature, continental serpentinization rates. *Geochimica et Cosmochimica Acta*, *347*, 1–15. https://doi.org/10.1016/j.gca.2023.02.008

Li, C., Li, Z., Peng, Z., Zhang, C., Nakata, N., & Sickbert, T. (2018). Long-period long-duration events detected by the IRIS community wavefield demonstration experiment in Oklahoma: Tremor or train signals? *Seismological Research Letters*, *89*(5), 1652–1659. https://doi.org/10.1785/0220180081

Lipovsky, B. P., & Dunham, E. M. (2015). Vibrational modes of hydraulic fractures: Inference of fracture geometry from resonant frequencies and attenuation. *Journal of Geophysical Research: Solid Earth*, *120*(2), 1080–1107. https://doi.org/10.1002/2014JB011286

Liu, T., & Mellon, B. (2026). SerpRateAI/oman_microearthquakes: Software for analyzing harmonic-tremor signals observed at the OmanDP MBO (version v0.0.1) [Software]. *Zenodo*. https://doi.org/10.5281/ZENODO.18891667

Lods, G., Roubinet, D., Matter, J. M., Leprovost, R., & Gouze, P. (2020). Groundwater flow characterization of an ophiolitic hard-rock aquifer from cross-borehole multi-level hydraulic experiments. *Journal of Hydrology*, *589*, 125152. https://doi.org/10.1016/j.jhydrol.2020.125152

Maher, S., Glasgow, M., Cochran, E., & Peng, Z. (2024). Distinguishing natural sources from anthropogenic noise in seismic data. https://doi.org/10.31223/X59Q6Q

Marcillo, O. E., & Carmichael, J. (2018). The detection of wind-turbine noise in seismic records. *Seismological Research Letters*, *89*(5), 1826–1837. https://doi.org/10.1785/0220170271

Marcillo, O. E., & MacCarthy, J. (2020). Mapping seismic tonal noise in the contiguous United States. *Seismological Research Letters*, *91*(3), 1707–1716. https://doi.org/10.1785/0220190355

Maryanto, S., Iguchi, M., & Tameguri, T. (2008). Constraints on the source mechanism of harmonic tremors based on seismological, ground deformation, and visual observations at sakurajima volcano, Japan. *Journal of Volcanology and Geothermal Research*, *170*(3–4), 198–217. https://doi.org/10.1016/j.jvolgeores.2007.10.004

Meng, H., & Ben-Zion, Y. (2018). Characteristics of airplanes and helicopters recorded by a dense seismic array near Anza California. *Journal of Geophysical Research: Solid Earth*, *123*(6), 4783–4797. https://doi.org/10.1029/2017JB015240

Moretti, I., Prinzhofer, A., Françolin, J., Pacheco, C., Rosanne, M., Rupin, F., & Mertens, J. (2021). Long-term monitoring of natural hydrogen superficial emissions in a Brazilian cratonic environment. Sporadic large pulses versus daily periodic emissions. *International Journal of Hydrogen Energy*, *46*(5), 3615–3628. https://doi.org/10.1016/j.ijhydene.2020.11.026

Nava, F. A., Ávila-Barrientos, L., Espíndola, J. M., & Núñez-Cornú, F. J. (2023). Volcanic harmonic tremor location. *Journal of Volcanology and Geothermal Research*, *444*, 107944. https://doi.org/10.1016/j.jvolgeores.2023.107944

Nayak, A., Manga, M., Hurwitz, S., Namiki, A., & Dawson, P. B. (2020). Origin and properties of hydrothermal tremor at lone star geyser, Yellowstone National Park, USA. *Journal of Geophysical Research: Solid Earth*, *125*(12), e2020JB019711. https://doi.org/10.1029/2020JB019711

Niyogi, S., Ghosh, A., Kumar, A., & Hammack, R. W. (2023). Tremor signals during fluid injection are generated by fault slip. *Science*, *381*(6657), 553–558. https://doi.org/10.1126/science.adh1331

Nothaft, D. B. (2021). Geologic map of the samail ophiolite, Oman and United Arab Emirates [Dataset]. *University of Colorado*. https://doi.org/10.25810/80W8-V777

Nothaft, D. B., Templeton, A. S., Boyd, E. S., Matter, J. M., Stute, M., & Paukert Vankeuren, A. N., & The Oman Drilling Project Science Team. (2021). Aqueous geochemical and microbial variation across discrete depth intervals in a peridotite aquifer assessed using a packer system in the samail ophiolite, Oman. *Journal of Geophysical Research: Biogeosciences*, *126*(9), e2021JG006319. https://doi.org/10.1029/2021JG006319

Osselin, F., Soulaine, C., Fauguerolles, C., Gaucher, E. C., Scaillet, B., & Pichavant, M. (2022). Orange hydrogen is the new green. *Nature Geoscience*, *15*(10), 765–769. https://doi.org/10.1038/s41561-022-01043-9

Pasquet, G., Loiseau, K., Diatta, M., Firpo, G., Swire, P., Amey, A., et al. (2024). Natural hydrogen in the northern semail ophiolite: A case study in the emirate of Ras Al Khaimah, UAE. *International Journal of Hydrogen Energy*, *110*, 787–796. https://doi.org/10.1016/j.ijhydene.2025.02.259

Rempfert, K. R., Miller, H. M., Bompard, N., Nothaft, D., Matter, J. M., Kelemen, P., et al. (2017). Geological and geochemical controls on subsurface microbial life in the samail ophiolite, Oman. *Frontiers in Microbiology*, *8*. https://doi.org/10.3389/fmicb.2017.00056

Röösli, C., Walter, F., Husen, S., Andrews, L. C., Lüthi, M. P., Catania, G. A., & Kissling, E. (2014). Sustained seismic tremors and icequakes detected in the ablation zone of the Greenland ice sheet. *Journal of Glaciology*, *60*(221), 563–575. https://doi.org/10.3189/2014JoG13J210

Schlindwein, V., Wassermann, J., & Scherbaum, F. (1995). Spectral analysis of harmonic tremor signals at Mt. Semeru volcano, Indonesia. *Geophysical Research Letters*, *22*(13), 1685–1688. https://doi.org/10.1029/95GL01433

Sohn, R. A. (2022). Oman borehole project land stations. *International Federation of Digital Seismograph Networks*. https://doi.org/10.7914/SN/7F_2019

Sohn, R. A., & Matter, J. M. (2023). The response of borehole water levels in an ophiolitic, peridotite aquifer to atmospheric, solid Earth, and ocean tides. *Journal of Hydrology X*, *21*, 100163. https://doi.org/10.1016/j.hydroa.2023.100163

St-Onge, A., & Eaton, D. W. (2011). Noise examples from two microseismic datasets. *CSEG Recorder*, *36*(10).

Tary, J. B., Van Der Baan, M., & Eaton, D. W. (2014). Interpretation of resonance frequencies recorded during hydraulic fracturing treatments. *Journal of Geophysical Research: Solid Earth*, *119*(2), 1295–1315. https://doi.org/10.1002/2013JB010904

Templeton, A. S., & Caro, T. A. (2023). The rock-hosted biosphere. *Annual Review of Earth and Planetary Sciences*, *51*(1), 493–519. https://doi.org/10.1146/annurev-earth-031920-081957

Templeton, A. S., Ellison, E. T., Kelemen, P. B., Leong, J., Boyd, E. S., Colman, D. R., & Matter, J. M. (2024). Low-temperature hydrogen production and consumption in partially-hydrated peridotites in Oman: Implications for stimulated geological hydrogen production. *Frontiers in Geochemistry*, *2*, 1366268. https://doi.org/10.3389/fgeoc.2024.1366268

Thomson, D. J. (1982). Spectrum estimation and harmonic analysis. *Proceedings of the IEEE*, *70*(9), 1055–1096. https://doi.org/10.1109/PROC.1982.12433

Winberry, J. P., Anandakrishnan, S., Wiens, D. A., & Alley, R. B. (2013). Nucleation and seismic tremor associated with the glacial earthquakes of whillans ice stream, Antarctica. *Geophysical Research Letters*, *40*(2), 312–315. https://doi.org/10.1002/grl.50130

Xia, J., & Miller, R. D. (2000). Design of a hum filter for suppressing power-line noise in seismic data. *Journal of Environmental & Engineering Geophysics*, *5*(2), 31–38. https://doi.org/10.4133/JEEG5.2.31

Zgonnik, V. (2020). The occurrence and geoscience of natural hydrogen: A comprehensive review. *Earth-Science Reviews*, *203*, 103140. https://doi.org/10.1016/j.earscirev.2020.103140